

Isogeometric shape optimisation of shell structures using multiresolution subdivision surfaces

Kosala Bandara, Fehmi Cirak*

Department of Engineering, University of Cambridge, Trumpington Street, Cambridge CB2 1PZ, U.K.

Abstract

We introduce the isogeometric shape optimisation of thin shell structures using subdivision surfaces. Both triangular Loop and quadrilateral Catmull-Clark subdivision schemes are considered for geometry modelling and finite element analysis. A gradient-based shape optimisation technique is implemented to minimise compliance, i.e. to maximise stiffness. Different control meshes describing the same surface are used for geometry representation, optimisation and finite element analysis. The finite element analysis is performed with subdivision basis functions corresponding to a sufficiently refined control mesh. During iterative shape optimisation the geometry is updated starting from the coarsest control mesh and proceeding to increasingly finer control meshes. This multiresolution approach provides a means for regularising the optimisation problem and prevents the appearance of sub-optimal jagged geometries with fine-scale oscillations. The finest control mesh for optimisation is chosen in accordance with the desired smallest feature size in the optimised geometry. The proposed approach is applied to three optimisation examples, namely a catenary, a roof over a rectangular domain and a freeform architectural shell roof. The influence of the geometry description and the used subdivision scheme on the obtained optimised curved geometries is investigated in detail.

Keywords: shape optimisation, thin shells, isogeometric analysis, subdivision surfaces, finite elements

1. Introduction

Shell structures are curved solids with one dimension significantly smaller than the other two. They are prevalent in many engineering applications, most prominently in aerospace, automotive and structural engineering. The load carrying capacity of shells can be greatly increased by systematically optimising their curved shape. Due to their small thickness the mechanics of shells can be efficiently described with surface models. The mechanical response of a thin shell depends, according to the Kirchhoff-Love model, on the first and second fundamental forms of the surface. In shape optimisation of shells, the efficient and flexible description of freeform surfaces and the finite element discretisation of the governing equations defined on them are intrinsically linked. In this paper we use the subdivision surfaces as a common representation for geometric modelling and finite element discretisation of Kirchhoff-Love shell equations.

Isogeometric analysis aims to unify geometric modelling and finite element analysis by using for the latter usual computer-aided design (CAD) basis functions, like NURBS. Since its inception by Hughes et al. [1, 2] isogeometric analysis has become immensely popular and has been applied to a wide range of engineering problems, too many to list here. Prior to the advent of isogeometric analysis, the integrated geometric modelling and finite element analysis of shells using subdivision surfaces was proposed in [3]. Specifically, Loop subdivision

surfaces were used for discretising the Kirchhoff-Love shells and representing their geometry. As an extension of this approach, the treatment of industrially prevalent non-manifold shell geometries and the inclusion of out-of-plane shear deformations relevant for thicker shells were proposed in [4] and [5], respectively. More recently the isogeometric analysis of shells and beams using NURBS basis functions were introduced in [6, 7]. The use of smooth subdivision and NURBS basis functions has also the advantage that they have square-integrable curvatures, which is necessary for discretising the Kirchhoff-Love shell equations depending on curvatures.

In the present work, we investigate the gradient-based shape optimisation of shell structures using subdivision surfaces for geometric modelling and finite element analysis. The minimised cost function is the compliance so that (qualitatively) displacements, strains and stresses are minimised. In a typical industrial design setting both the input to and output from structural optimisation is a geometry, i.e. a CAD model. During optimisation the cost function and its derivatives with respect to some geometric design parameters, i.e. design sensitivities, need to be computed with finite element analysis [8, 9]. Hence, as a matter of fact, the interoperability of geometry and finite element models is crucial. Equally important are techniques for choosing suitable geometric design variables that can parameterise a sufficiently large set of geometries. Over the years, a wide variety of shape parameterisation techniques have been proposed that are based either on a CAD, a finite element analysis (FEA) or an intermediary model [10, 11]. In one group of techniques the geometric design variables are the parameters of the CAD

*Corresponding author

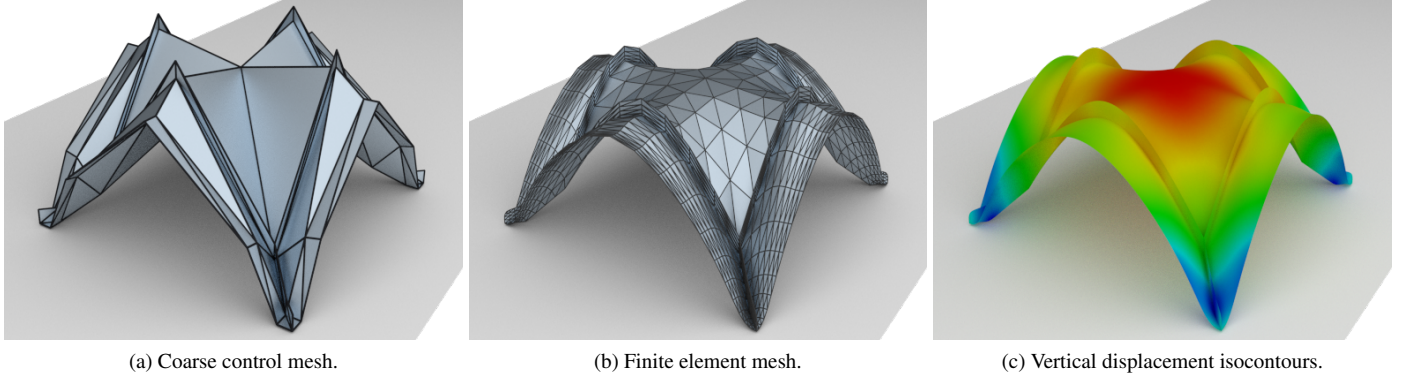


Figure 1: Shape optimised thin shell roof structure emanating from a flat plate with stiffeners. The structure is loaded with a uniformly distributed vertical load and is supported at its four corners. The vertex positions of the coarse control mesh (a) represent the optimisation design variables. The compliance cost function and its derivatives are evaluated with finite element analysis using the twice subdivided control mesh (b) and the corresponding smooth subdivision basis functions. The limit surface and the isocontours of the vertical displacement are shown in (c).

model or a reconstructed CAD-like spline model [12–16]. In the second group of techniques the design variables are the vertex positions of the finite element mesh [17–19]. Yet in another group of parameterisation techniques, like the ones based on radial basis functions [20] or free-form deformations [21, 22], the design variables are only indirectly linked to the CAD or FEA model. This list of parameterisation techniques is not intended to be complete. The abundance of shape parameterisation techniques is partly due to the inherent limitations and incompatibilities of conventional CAD and FEA models in the context of shape optimisation. With isogeometric analysis using subdivision surfaces most of the incompatibilities between the CAD and FEA representations can be elegantly circumvented. To this end, the increasing availability of subdivision surfaces in CAD systems, including PTC Creo, CATIA, Siemens NX or Autodesk Fusion 360, is noteworthy.

In isogeometric shape optimisation with subdivision surfaces different resolutions, i.e. control meshes, of a surface are employed for optimisation and performing the finite element analysis, see Figure 1. In computer graphics subdivision surfaces are usually viewed as a process for generating increasingly finer meshes that converge in the limit to a surface [23]. Alternatively, they can be viewed as a generalisation of splines to arbitrary connectivity meshes [24]. In the proposed optimisation approach, both viewpoints are simultaneously exploited. Subdivision surfaces are best considered as generalised splines when used as finite element basis functions. On the other hand, the discrete computer graphics viewpoint with the associated data structures and algorithms is best suited for simultaneously operating on different resolutions in a memory and time efficient manner. Our present implementation is based on the triangular Loop [25] and quadrilateral Catmull-Clark schemes [26], or more specifically on their extended versions introduced in [27]. The finite element analysis is performed with basis functions corresponding to a sufficiently fine control mesh. Within the optimisation loop, starting with the coarsest, the vertex positions of increasingly finer control meshes are used as design variables. The resolution of the control mesh determines the extent of applied geometry changes, because each

vertex has control over the surface within a two-ring of adjacent elements. The derivatives of the cost function with respect to vertex positions is first computed on the fine finite element control mesh and subsequently projected to the coarser control meshes corresponding to the design variables. This projection provides a means for smoothing, or filtering, of the computed design sensitivities and prevents the appearance of jagged optimised geometries with fine-scale oscillations. The need for such a smoothing, or filtering, in shape optimisation is widely discussed in literature, see e.g. [17, 19] and references therein.

An earlier two-level version of the multiresolution optimisation approach proposed in this paper was introduced in [28]. In that exploratory work Loop subdivision and non-gradient based optimisation algorithms were used. More recently the proposed multiresolution approach has been applied to other types of optimisation problems, namely electrostatic shape optimisation of high-voltage devices [29] and shape optimisation of volumetric solids [30]. The electrostatic simulations are performed with the boundary element method and the solid simulations with the voxel-based immersed finite element method.

This paper is organised as follows. In Section 2 we begin by reviewing the Kirchhoff-Love model for thin shells and its discretisation with subdivision basis functions. We then introduce the compliance optimisation problem and compute with an adjoint approach the cost function derivatives with respect to the vertex positions of the subdivision control mesh. Section 3 provides a very brief introduction to subdivision surfaces. Subsequently, in Section 4 the multiresolution algorithm is introduced. Finally, in Section 5 we introduce three examples of increasing complexity, namely the shape optimisation of a thin-strip, a roof over a rectangular domain and a freeform architectural shell roof.

2. Thin-shells

2.1. Governing equations and discretisation

We consider a thin-shell with the undeformed mid-surface Ω and the thickness t , see Figure 2. The surface Ω is parameterised with the curvilinear coordinates $(\theta^1, \theta^2) \in \mathbb{R}^2$ providing

each material point on the surface with a unique parametric coordinate. The position of the material points is denoted with the coordinates $\mathbf{x}(\theta^1, \theta^2) \in \mathbb{R}^3$.

The standard covariant basis vectors of the mid-surface \mathbf{a}_α and the unit normal \mathbf{a}_3 are given by

$$\mathbf{a}_\alpha = \frac{\partial \mathbf{x}}{\partial \theta^\alpha} = \mathbf{x}_{,\alpha}, \quad \mathbf{a}_3 = \frac{\mathbf{a}_1 \times \mathbf{a}_2}{|\mathbf{a}_1 \times \mathbf{a}_2|}. \quad (1)$$

The corresponding contravariant basis vectors \mathbf{a}^α are defined through the relation $\mathbf{a}^\alpha \cdot \mathbf{a}_\beta = \delta_\beta^\alpha$, where δ_β^α is the Kronecker delta. Here and in the following the Greek indices take the values $\{1, 2\}$ and the summation convention is used.

Displacing each material point on the mid-surface with a displacement vector $\mathbf{u}(\theta^1, \theta^2) \in \mathbb{R}^3$ yields a deformed (or, displaced) mid-surface. Subject to few mechanical assumptions, it can be shown that the differences in the first and second fundamental forms of the original and displaced surface provide suitable strain measures. The difference in the first fundamental form is referred to as the membrane strain tensor $\boldsymbol{\alpha}$ and the difference in the second fundamental form as the bending strain tensor $\boldsymbol{\beta}$. In case of small displacements, as derived e.g. in [3], the linearised membrane strain tensor is

$$\boldsymbol{\alpha} = \frac{1}{2} (\mathbf{a}_{\alpha,\beta} \cdot \mathbf{u}_{,\beta} + \mathbf{u}_{,\alpha} \cdot \mathbf{a}_{\beta}) \mathbf{a}^\alpha \otimes \mathbf{a}^\beta \quad (2)$$

and the linearised bending strain tensor is

$$\begin{aligned} \boldsymbol{\beta} = & \left(-\mathbf{u}_{,\alpha\beta} \cdot \mathbf{a}_3 + \frac{1}{\sqrt{a}} [\mathbf{u}_{,1} \cdot (\mathbf{a}_{\alpha\beta} \times \mathbf{a}_2) + \mathbf{u}_{,2} \cdot (\mathbf{a}_1 \times \mathbf{a}_{\alpha\beta})] \right. \\ & \left. + \frac{\mathbf{a}_3 \cdot \mathbf{a}_{\alpha\beta}}{\sqrt{a}} [\mathbf{u}_{,1} \cdot (\mathbf{a}_2 \times \mathbf{a}_3) + \mathbf{u}_{,2} \cdot (\mathbf{a}_3 \times \mathbf{a}_1)] \right) \mathbf{a}^\alpha \otimes \mathbf{a}^\beta \end{aligned} \quad (3)$$

with $\sqrt{a} = |\mathbf{a}_1 \times \mathbf{a}_2|$.

Next, we consider the potential energy of the displaced shell

$$\begin{aligned} \Pi(\mathbf{u}) = & \int_{\Omega} (W^m(\boldsymbol{\alpha}) + W^b(\boldsymbol{\beta})) d\Omega - \int_{\Omega} \mathbf{p} \cdot \mathbf{u} d\Omega \\ & - \int_{\Gamma} \mathbf{r} \cdot \mathbf{u} d\Gamma, \end{aligned} \quad (4)$$

where the first integral is the internal potential energy consisting of the sum of the internal membrane and bending energy densities W^m and W^b , respectively. The remaining two integrals represent the external potential energy resulting from the prescribed surface load vector \mathbf{p} and the edge load vector \mathbf{r} . For an elastic material the two internal energy densities are defined with

$$\begin{aligned} W^m(\boldsymbol{\alpha}) = & \frac{1}{2} \frac{Et}{1-\nu^2} \boldsymbol{\alpha} : \mathbf{H} : \boldsymbol{\alpha} \\ W^b(\boldsymbol{\beta}) = & \frac{1}{2} \frac{Et^3}{12(1-\nu^2)} \boldsymbol{\beta} : \mathbf{H} : \boldsymbol{\beta}, \end{aligned} \quad (5)$$

where E is the Young's modulus, ν is the Poisson's ratio and $\mathbf{H} = H^{\alpha\beta\gamma\delta} \mathbf{a}_\alpha \otimes \mathbf{a}_\beta \otimes \mathbf{a}_\gamma \otimes \mathbf{a}_\delta$ is an auxiliary fourth order tensor with the contravariant components

$$H^{\alpha\beta\gamma\delta} = \nu a^{\alpha\beta} a^{\gamma\delta} + \frac{1}{2} (1-\nu) (a^{\alpha\gamma} a^{\beta\delta} + a^{\alpha\delta} a^{\beta\gamma}) \quad (6)$$

and the contravariant metric $a^{\alpha\beta} = \mathbf{a}^\alpha \cdot \mathbf{a}^\beta$.

The equilibrium configurations of the shell with prescribed loading are obtained from minimising (4). Note that for a well-posed problem also the displacements on some parts of the boundary have to be prescribed in addition to the loading. In a finite element approximation, the mid-surface position and the displacement vectors in (4) are approximated with basis functions and their coefficients

$$\mathbf{x}(\theta^1, \theta^2) \approx \sum_i N_i(\theta^1, \theta^2) \mathbf{x}_i, \quad \mathbf{u}(\theta^1, \theta^2) \approx \sum_i N_i(\theta^1, \theta^2) \mathbf{u}_i. \quad (7)$$

In our implementation, the basis functions $N_i(\theta^1, \theta^2)$ are obtained either from triangular Loop subdivision or quadrilateral Catmull-Clark subdivision. In both schemes there is one basis function associated with each vertex of the control mesh. Hence, the coefficients \mathbf{x}_i and \mathbf{u}_i are simply the position and displacements of a (control) vertex with the index i . Introducing the approximations (7) into the potential (4) yields a discrete minimisation problem for computing the vertex displacements \mathbf{u}_i ,

$$\mathbf{u}_i = \arg \min_{\mathbf{u}_i} \Pi(\mathbf{u}_i) \Rightarrow \frac{\partial \Pi(\mathbf{u}_i)}{\partial \mathbf{u}_i} = \mathbf{0}. \quad (8)$$

In order to compute the stationary points of $\Pi(\mathbf{u}_i)$ domain integrals are numerically evaluated in a usual finite element fashion by iterating over the elements/faces in the control mesh. Around extraordinary vertices subdivision surfaces consist of an infinite sequence of ever smaller rings of box splines in Loop subdivision and b-splines in Catmull-Clark subdivision [24]. Hence, their numerical integration requires special care and has been investigated in several recent numerical studies [31, 32]. For practical computations, the integration of each finite element using Gauss integration with 3 points for Loop subdivision and 4 points for Catmull-Clark subdivision appears to provide the best trade-off between accuracy and robustness [5, 32]. As an aside, the issue of accuracy of quadrature is independent from the sub-optimal convergence of finite elements based on subdivision surfaces, which is presently a very active area of research, see [33] and the references therein. At the Gauss points, we evaluate the basis functions with a simplified version of the algorithm proposed by Stam [34, 35], see [3, 4]. Specifically, since the Gauss points are relatively far from extraordinary vertices there are no efficiency gains from the eigendecomposition considered in [34, 35]. After numerical integration the stationarity condition for the minimisation problem (8) yields a discrete system of equations

$$\frac{\partial \Pi(\mathbf{u}_i)}{\partial \mathbf{u}_i} = \mathbf{0} \Rightarrow \mathbf{K} \mathbf{u} = \mathbf{f}, \quad (9)$$

where \mathbf{K} is the symmetric, positive-definite system (or, stiffness) matrix, \mathbf{u} is the array of vertex displacements containing all \mathbf{u}_i and \mathbf{f} is the array of corresponding vertex forces. For further details see [3, 28].

2.2. Design sensitivities

In shape optimisation we consider a shell structure with prescribed loading and displacement boundary conditions and aim

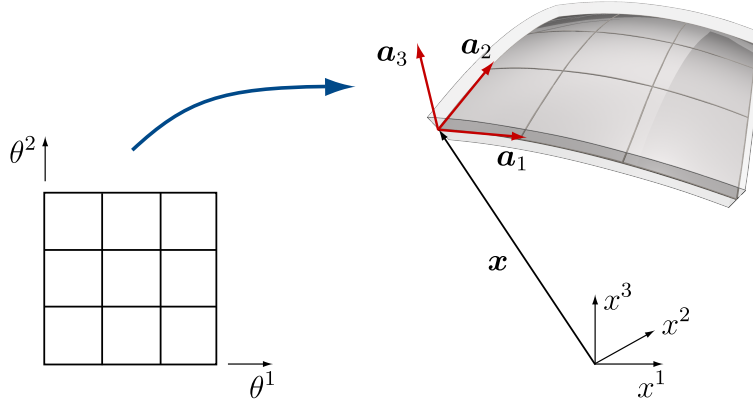


Figure 2: Solid thin-shell and its mid-surface (right) with the position vector $\mathbf{x}(\theta^1, \theta^2)$, the covariant basis vectors \mathbf{a}_1 and \mathbf{a}_2 , and the normal vector \mathbf{a}_3 . The parameter space with the coordinates (θ^1, θ^2) is shown on the left.

to find its mid-surface such that a user chosen cost function

$$\min_{\mathbf{x}} J(\mathbf{x}, \mathbf{u}) \quad (10)$$

is minimised. As a constraint the array of the vertex displacements \mathbf{u} has to satisfy the equilibrium equations (9). In practice, there are additional constraints, for instance pertaining to the surface area of the shell or the position of selected vertices, which will be omitted in this section. Moreover, in all examples presented in this paper the cost function is the compliance of the structure

$$J(\mathbf{x}, \mathbf{u}) = \mathbf{u}^T \mathbf{f} = \mathbf{u}^T \mathbf{K} \mathbf{u}. \quad (11)$$

Informally, minimising the compliance leads to stiffer shell structures with smaller displacements \mathbf{u} . The subsequent derivations carry over to other cost functions, see e.g. [8].

In order to use a gradient-based optimisation algorithm for minimising $J(\mathbf{x}, \mathbf{u})$ the derivatives of the cost function with respect to the vertex coordinates, also referred to as design sensitivities or shape gradients, are needed. To this end, we consider the adjoint formulation with

$$L(\mathbf{x}, \mathbf{u}, \lambda) = J(\mathbf{x}, \mathbf{u}) + \lambda^T [\mathbf{f} - \mathbf{K} \mathbf{u}] = \mathbf{u}^T \mathbf{K} \mathbf{u} + \lambda^T [\mathbf{f} - \mathbf{K} \mathbf{u}], \quad (12)$$

where λ is an array of Lagrange parameters. The stationarity condition for $L(\mathbf{x}, \mathbf{u}, \lambda)$ with respect to the vertex displacements leads to the adjoint problem

$$\frac{\partial L(\mathbf{x}, \mathbf{u}, \lambda)}{\partial \mathbf{u}} = \mathbf{0} \quad \Rightarrow \quad \mathbf{K} \lambda = 2 \mathbf{K} \mathbf{u} \quad \Rightarrow \quad \lambda = 2 \mathbf{u}. \quad (13)$$

Here, we made use of the symmetry of the stiffness matrix \mathbf{K} . The equality between the Lagrange parameters λ and displacements \mathbf{u} (up to the constant 2) is only valid when the cost function is the compliance (11). The stationarity condition for $L(\mathbf{x}, \mathbf{u}, \lambda)$ with respect to the vertex coordinates leads to the design sensitivities

$$\frac{\partial L(\mathbf{x}, \mathbf{u}, \lambda)}{\partial \mathbf{x}} = \mathbf{u}^T \frac{\partial \mathbf{K}}{\partial \mathbf{x}} \mathbf{u} + 2 \mathbf{u}^T \left[\frac{\partial \mathbf{f}}{\partial \mathbf{x}} - \frac{\partial \mathbf{K}}{\partial \mathbf{x}} \mathbf{u} \right] \quad (14)$$

$$= 2 \mathbf{u}^T \frac{\partial \mathbf{f}}{\partial \mathbf{x}} - \mathbf{u}^T \frac{\partial \mathbf{K}}{\partial \mathbf{x}} \mathbf{u}. \quad (15)$$

At equilibrium, that is when $\mathbf{K} \mathbf{u} - \mathbf{f} = \mathbf{0}$ is exactly satisfied, the gradients of the Lagrangian $L(\mathbf{x}, \mathbf{u}, \lambda)$ and the cost function $J(\mathbf{x}, \mathbf{u})$ with respect to the vertex coordinates are identical. Hence, in gradient-based shape optimisation the vertex coordinates have to be perturbed in the direction

$$\mathbf{v} = -2 \mathbf{u}^T \frac{\partial \mathbf{f}}{\partial \mathbf{x}} + \mathbf{u}^T \frac{\partial \mathbf{K}}{\partial \mathbf{x}} \mathbf{u}. \quad (16)$$

to achieve a decrease in the cost function. In order to compute \mathbf{v} the derivatives of the load vector \mathbf{f} and system (or stiffness) matrix \mathbf{K} with respect to the vertex coordinates \mathbf{x} are needed. For the considered Kirchhoff-Love shell formulation it is straightforward to compute these derivatives by systematic element-by-element differentiation of the discrete equilibrium equations (9). Note that other shell formulations, especially ones available in commercial software, contain as degrees of freedom in addition to vertex positions also the rotations of vertex director vectors. This usually makes the computation of the related design sensitivities more complex.

3. Subdivision surfaces

In the isogeometric analysis context it is expedient to consider subdivision surfaces as the generalisation of splines to arbitrary connectivity meshes [23, 24]. As known, refinable basis functions allow to represent the same spline surface with control meshes of different resolutions. Loop subdivision [25] is the generalisation of quartic box-splines to arbitrary connectivity triangular meshes and Catmull-Clark [26] subdivision is the generalisation of tensor-product cubic b-splines to arbitrary connectivity quadrilateral meshes. Both schemes lead to basis functions that are refinable.

The control meshes are refined by quadrissection of elements. In triangular Loop subdivision this is achieved by introducing a new vertex on each edge. In Catmull-Clark in addition to new vertices on the edges a new vertex at the centre of each element is created. The control vertex coordinates of a refined mesh at level $\ell + 1$ are obtained from the vertex coordinates of the coarse mesh at level ℓ according to

$$\mathbf{x}^{\ell+1} = \mathbf{S} \mathbf{x}^{\ell}. \quad (17)$$

For vertices located in the regular regions of a mesh the subdivision matrix \mathbf{S} contains the standard knot insertion weights. The matrix components associated to the vertices in the irregular regions and at the boundaries are given by the specific subdivision scheme. Explicit expressions for the subdivision matrix \mathbf{S} can be found, e.g., in [23]. The successive subdivision refinement of a control mesh can be interpreted as the chain of linear mappings

$$\mathbf{x}^0 \xrightarrow{\mathbf{S}} \mathbf{x}^1 \xrightarrow{\mathbf{S}} \mathbf{x}^2 \xrightarrow{\mathbf{S}} \dots \xrightarrow{\mathbf{S}} \mathbf{x}^{\ell-1} \xrightarrow{\mathbf{S}} \mathbf{x}^\ell. \quad (18)$$

The size of the vertex coordinates \mathbf{x}^ℓ increases with increasing ℓ and the size of the subdivision matrix \mathbf{S} increases accordingly. All control meshes converge irrespective of their level ℓ to the same surface. As mentioned in Section 2.1, the algorithm proposed by Stam [34, 35] provides a spline based parameterisation of subdivision surfaces so that the properties of arbitrary surface points can be evaluated, cf. (7). There are also alternative parameterisations available, see [31, 36, 37].

In shape optimisation the coarsening of the refined subdivision control meshes is also needed, that is,

$$\mathbf{x}^\ell = \mathbf{R} \mathbf{x}^{\ell+1} \quad \text{with} \quad \mathbf{R} = (\mathbf{S}^\top \mathbf{S})^{-1} \mathbf{S}^\top, \quad (19)$$

where the coarsening matrix \mathbf{R} is defined as the pseudo-inverse of the subdivision matrix \mathbf{S} . The span of geometries that can be represented with $\mathbf{x}^{\ell+1}$ is larger than the ones with \mathbf{x}^ℓ , hence the specific form of \mathbf{R} is a choice. As discussed in [29, 30], \mathbf{R} can be interpreted as a smoothing operator and accordingly different choices are possible. Similar to subdivision refinement the coarsening matrix can be successively applied in order to obtain coarser representations of the geometry, i.e.,

$$\mathbf{x}^0 \xleftarrow{\mathbf{R}} \mathbf{x}^1 \xleftarrow{\mathbf{R}} \mathbf{x}^2 \xleftarrow{\mathbf{R}} \dots \xleftarrow{\mathbf{R}} \mathbf{x}^{\ell-1} \xleftarrow{\mathbf{R}} \mathbf{x}^\ell. \quad (20)$$

Note that, by definition (19), one step of subdivision refinement followed by one step of coarsening does not change the vertex coordinates, or $\mathbf{R}\mathbf{S} = \mathbf{I}$.

4. Shape optimisation

The subdivision surfaces enable us to use different resolutions of the same geometry for optimisation and analysis. Crucially, in the spirit of isogeometric analysis the control meshes for analysis and optimisation represent the same surface. A simplified two-level version of the proposed iterative gradient-based optimisation algorithm is shown Algorithm 1. For a more advanced multiresolution version employing a wavelet-like decomposition of the surface, in the context of shape optimisation of solids, see [30]. The optimisation and analysis meshes correspond to different refinement levels in a subdivision hierarchy. The optimisation level is initialised with $\ell_o = 0$ and the analysis level is fixed with $\ell_c = n$, where n is user prescribed. The gradient of the compliance cost function \mathbf{v}^{ℓ_c} is computed with a finite element analysis using basis functions of the control

mesh at level ℓ_c , see Section 2. Subsequently, through successive multiplication of the gradient with the coarsening matrix \mathbf{R} the optimisation level gradient \mathbf{v}^{ℓ_o} is obtained. As indicated in Algorithm 1 the updated coordinates \mathbf{x}^{ℓ_o} of the optimisation level can be, for instance, obtained with a simple steepest descent method. Instead of this simple update algorithm, we use in the presented examples the MMA optimisation algorithm in the NLOpt library [38]. The MMA algorithm usually requires fewer iterations to converge and is able to consider both equality and inequality side constraints. Moreover, in the presented examples the optimisation level is successively increased every time a stationary point is reached until a user prescribed maximum optimisation level is reached. It is evident that $\ell_o \leq \ell_c$. The termination criterion for optimisation iterations is tightened with increasing optimisation level ℓ_o . In the presented examples the tolerance parameter for the iterations is chosen to be $\varepsilon = 10^{-3(\ell_o+1)}$.

Algorithm 1 Multiresolution shape optimisation

```

// read maximum optimisation level  $\ell_{o,max}$ 
// read finite element analysis level  $\ell_c$ 
// read input coarse control mesh  $\mathbf{x}^0$ 
// initialise optimisation level
1:  $\ell_o = 0$ 
// initialise cost function
2:  $J = \infty$ 
// iterate over optimisation levels
3: while  $\ell_o \leq \ell_{o,max}$  do
    // update vertex coordinates  $\mathbf{x}^{\ell_o}$  while cost function decreases
4:   repeat
    // subdivide optimisation level  $\ell_o$  up to analysis level  $\ell_c$ 
5:     for  $\ell \leftarrow \ell_o$  to  $\ell_c - 1$  do
6:        $\mathbf{x}^{\ell+1} \leftarrow \mathbf{S} \mathbf{x}^\ell$ 
    // store previous cost function
7:      $J_{previous} \leftarrow J$ 
    // compute cost function  $J = J(\mathbf{x}^{\ell_c}, \mathbf{u}^{\ell_c})$  and its gradient  $\mathbf{v}^{\ell_c}$ 
    // project gradient to optimisation level
8:     for  $\ell \leftarrow \ell_c$  to  $\ell_o + 1$  do
9:        $\mathbf{v}^{\ell-1} \leftarrow \mathbf{R} \mathbf{v}^\ell$ 
    // update vertex coordinates of the optimisation level
10:     $\mathbf{x}^{\ell_o} \leftarrow (\mathbf{x}^{\ell_o} + \alpha \mathbf{v}^{\ell_o})$  with  $\alpha \geq 0$ 
11:  until  $(J_{previous} - J) < \frac{\varepsilon}{2}(J_{previous} + J)$ 
    // increment optimisation level
12:   $\ell_o \leftarrow (\ell_o + 1)$ 

```

5. Examples

Three examples are presented to demonstrate the functioning of the proposed isogeometric shape optimisation of thin-shell structures using subdivision. In all examples the objective is to minimise the compliance. As subdivision schemes the triangular Loop and the quadrilateral Catmull-Clark scheme are used. In order to preserve corners and edges of the original geometry, at vertices and edges on the boundary modified subdivision stencils are applied [4, 27].

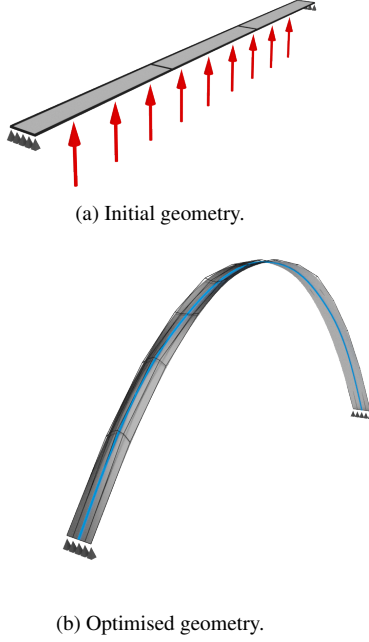


Figure 3: Optimisation of an uniformly loaded thin strip.

5.1. Thin strip

In this verification example, a thin strip pinned at both ends and subjected to a vertical distributed load is optimised, see Figure 3. Initially, the strip is a narrow flat plate with length 1 equal to the distance between the supports. The magnitude of the vertical uniformly distributed load is 1000. The width of the strip is 0.05; the thickness is 0.02; the Young's modulus is $E = 2 \times 10^8$; and the Poisson's ratio is $\nu = 0.3$.

The Catmull-Clark subdivision scheme is used for representing the geometry and finite element analysis. Although there are no extraordinary vertices in the control mesh, the subdivision basis functions are neither uniform nor non-uniform b-splines due to the treatment of the boundaries [27]. The initial coarse mesh used for optimisation contains only 3 elements along the length and 1 element across the width of the strip. This increases to 48 in the twice subdivided analysis fine mesh, i.e. $\ell_c \equiv 2$. During compliance optimisation the mesh resolution is increased starting from $\ell_o = 0$ up to $\ell_o = 2$. Only the out-of-plane position of the control points in the direction of the load vector are optimised. The length of the optimised strip is chosen to be either 1.1, 1.2 or 1.3 by prescribing its area, see [30] for the treatment of area constraints.

As known from classical mechanics, the shape of the curve assumed by a loose string pinned at both ends is a catenary curve [39], which is for the considered geometry of the form

$$y = c_1 \cdot \cosh(x/c_1) + c_2, \quad (21)$$

where the y -axis is parallel to the applied load vector and the left and right supports have the coordinates $(-0.5, 0)$ and $(0.5, 0)$,

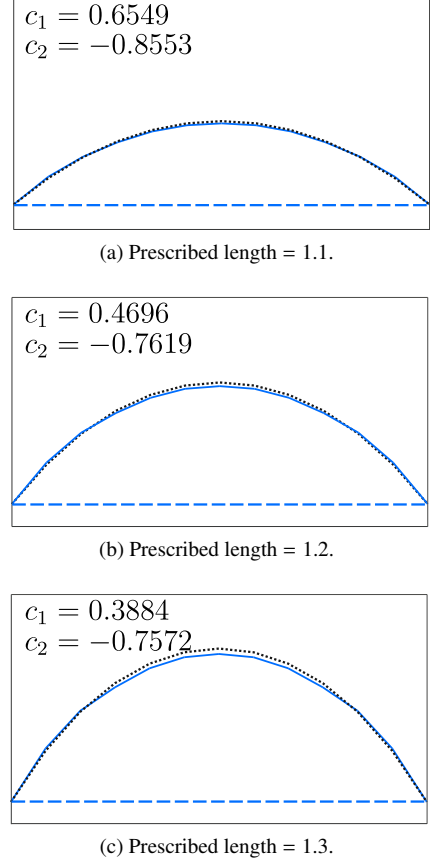


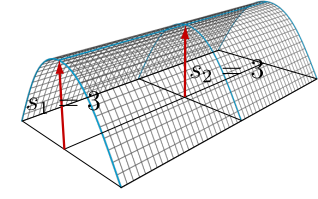
Figure 4: Optimisation of a thin strip with different prescribed lengths. The blue lines show the centre line of the strip before and after optimisation and the dotted black line is the catenary curve.

respectively. The constants c_1 and c_2 depend on the chosen length of the optimised strip. The comparison of the optimisation results with the corresponding catenary curves is shown in Figure 4. The reduction of the compliance cost function is more than 99.9% and the optimisation results show good visual agreement with the catenary curve. The slight deviation from the catenary is possibly due to the finite width of the strip, which leads during optimisation to some curvature generation across the width of the shell (visible in Figure 3b).

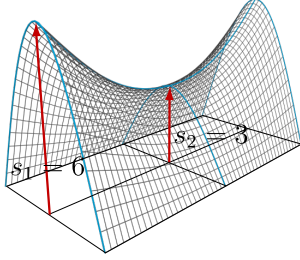
5.2. Shell roof over a rectangular domain

Our second example is adapted from Bletzinger et al. [13] and considers the compliance optimisation of a roof over a rectangular domain, see Figure 5. The roof has the plan of 6×12 and is pinned along its two long edges. The applied loading consists of a uniformly distributed vertical load of 5000. The shell thickness is $t = 0.05$; the Young's modulus is $E = 3 \times 10^{10}$; and the Poisson's ratio is $\nu = 0.2$. As indicated in Figure 5, Bletzinger et al. used only the two height parameters s_1 and s_2 to optimise the roof geometry while maintaining a bi-parabolic shape. Moreover, they chose a cylindrical shell as their initial shape prior to optimisation.

In the performed computations a flat rectangle with four different control mesh layouts is used as the initial geometry, see Figure 6. The aim of considering the different initial meshes is



(a) Initial geometry ($J(\mathbf{x}, \mathbf{u}) = 2108$).



(b) Optimised geometry ($J(\mathbf{x}, \mathbf{u}) = 149.68$)

Figure 5: Roof over a rectangular domain. Initial and optimised geometries from Bletzinger and Ramm [13]. The given compliance cost functions values are computed with the introduced thin-shell solver.

to highlight the mesh dependence of the optimised shape. With a gradient-based algorithm a certain mesh dependence of the optimisation results is unavoidable because most structural optimisation problems are non-convex and often not well-posed. In the computed four different cases, during optimisation only the out-of-plane position of vertices are modified with an prescribed upper bound of 6 in order to reproduce the effect of limiting the maximum height $s_1 \leq 6$ in [13]. In all cases the analysis level is chosen with $\ell_c \equiv 2$. The optimisation level starts with $\ell_o = 0$ and is incremented each time the cost function reaches a steady state as long as $\ell_o \leq \ell_c \equiv 2$. In Figure 6 the optimised geometries and the corresponding cost function values are shown. The given cost function values are obtained using a fine computational mesh, which has a comparable resolution in all four cases. For comparison, the cost function of the initial flat rectangular plate is $\approx 46 \times 10^4$. In all four cases a large reduction in the cost function is achieved and there are significant differences in the final geometries. Only starting off with very few optimisation variables in the initial coarse mesh, like in A, B and C, appears to give lower minima. Note also the resemblance of the optimised geometries for meshes A, B and C to the optimised geometry of Bletzinger et al. [13] shown in Figure 5b. In contrast to the geometry in Figure 5b, the results for meshes A and B have lower cost function values possibly due to the presence of the fine-scale ripples on the optimised geometries that can be seen in Figure 6, first, second and third columns.

The choice of the optimisation and computational levels ℓ_o and ℓ_c is studied next, see Figure 7. In one set of computations, referred to as *single-resolution optimisation*, the two levels are chosen to be the same $\ell_o \equiv \ell_c$. This means the opti-

misation variables are simply the out-of-plane positions of the vertices of the computational mesh. In a second set of computations, referred to as *multiresolution optimisation*, the optimisation level always starts with $\ell_o = 0$ and is successively incremented as long as $\ell_o \leq \ell_c$, as discussed in the preceding paragraph. The obtained cost functions for the two different optimisation strategies and for $\ell_c \in \{0, 1, 2, 3, 4\}$ are plotted in Figure 7. In the cost function plot each point represents one independent optimisation problem. For all problems the initial control mesh is the quadrilateral mesh A shown in Figure 6. Note that as expected the result for the multiresolution optimisation for large $\ell_c \geq 2$ is the same as in Figure 6, first column. In contrast, for single-resolution optimisation the obtained geometries become highly oscillatory when the level $\ell_o \equiv \ell_c$ is increased. This is a well-known problem in shape optimisation and suggests the ill-posedness of the optimisation problem requiring some form of regularisation [12]. In multiresolution optimisation the design sensitivities are computed on the fine control mesh and are subsequently projected to the coarser optimisation control mesh using the coarsening matrix \mathbf{R} . As in established smoothing, or filtering, techniques in shape optimisation [17, 19], the projection of the design sensitivities leads to a smoothing of the design sensitivities. The lack of a projection, and hence a smoothing, in single-resolution optimisation appears to be the cause of the appearance of the non-optimal jagged geometries with fine-scale oscillations. In Figure 7 all the given cost functions are obtained using a fine control mesh with the same resolution for all data points.

5.3. Freeform architectural shell roof

In design practice, such as in architectural engineering, in addition to structural efficiency there are a number of equally important, often not explicitly quantifiable, design objectives. Although there is a dearth of research on the use of optimisation in a professional design setting, a recent study shows that designers usually use optimisation for generating ideas, that is to discover new and unexpected geometries, and do not see it as a means for generating the ultimate design [40]. With this in mind, isogeometric shape optimisation can aid the designers in search for structurally efficient geometries that satisfy all design objectives. An efficient shell structure can be generated by intermittently shape optimising and manually editing the control mesh vertex positions and increasing or decreasing the refinement level. That is, the designer can consult shape optimisation throughout the entire design stage as often as needed. This sketched design workflow is only feasible with isogeometric analysis and the afforded tight link between the geometry and analysis models.

To illustrate the use of multiresolution optimisation in a more realistic design setting we consider the roof structure shown in Figure 8. The approximate dimensions of the shell structure are $2.31 \times 6.27 \times 0.75$. It is supported only at three points and contains at the top an opening for lighting purposes and a crease (G^0 -continuous feature line). The applied loading consists of a uniformly distributed load of -1000 (downwards). The shell thickness is $t = 0.02$; the Young's modulus is $E = 10^{10}$; and the Poisson's ratio is $\nu = 0.2$. The triangular control mesh with 26

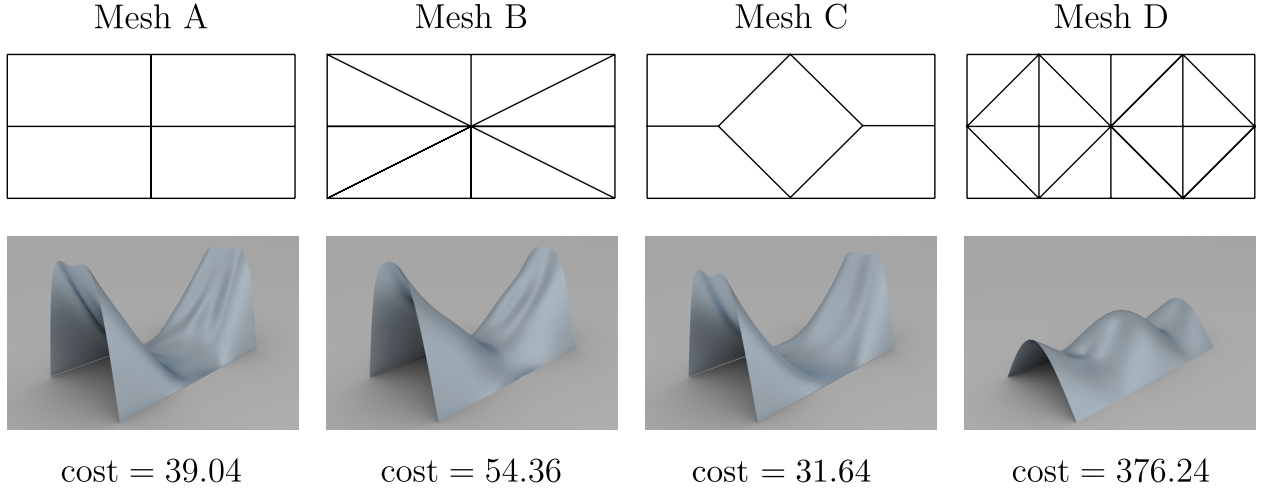


Figure 6: Roof over a rectangular domain with four different coarse control meshes. Each column shows the coarse control mesh, the obtained optimised geometry and the corresponding cost function value. The analysis level is chosen with $\ell_c \equiv 2$. The optimisation level starts with $\ell_o = 0$ and is incremented while $\ell_o \leq \ell_c$.

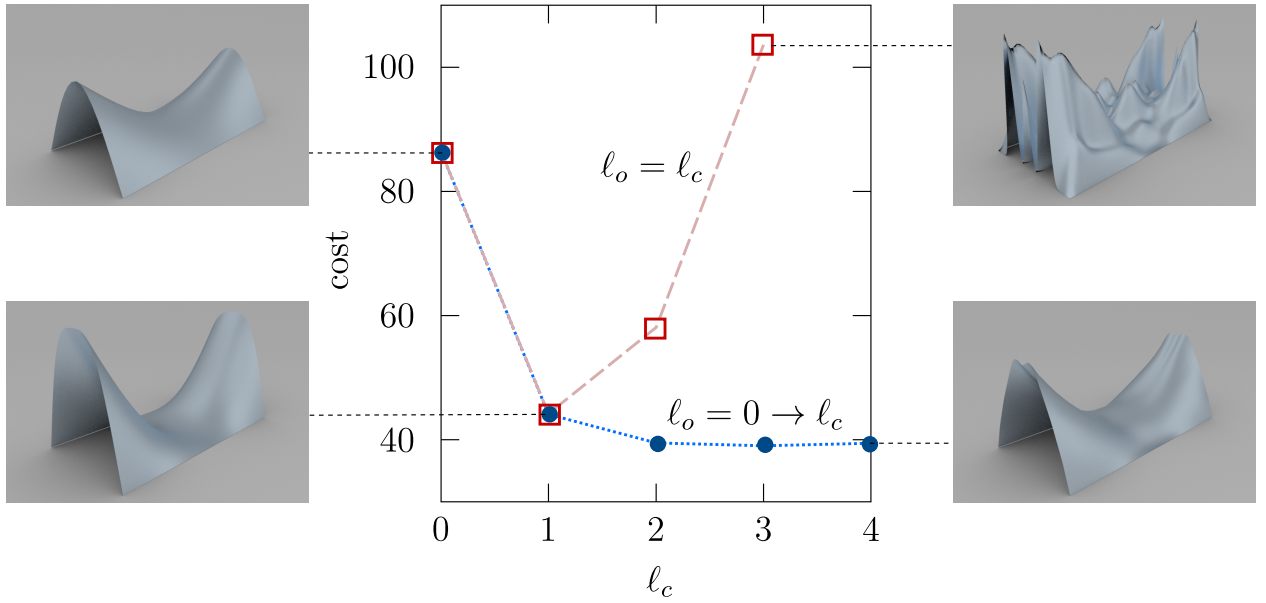


Figure 7: Comparison of single-resolution and multiresolution optimisation for a roof over a rectangular domain. The coarse control mesh in all cases is the quadrilateral mesh A shown in Figure 6. The dashed red line indicates single resolution optimisation with $\ell_o \equiv \ell_c$. The dotted blue line indicates multiresolution optimisation, which starts with optimisation level $\ell_o = 0$ and is incremented while $\ell_o \leq \ell_c$. Each data point in the plot denotes the final cost of an independent optimisation study. Inset pictures are the optimised shapes at the indicated data points.

	Labels of the fixed vertices
Design A	square, filled diamond, empty diamond
Design B	square, filled diamond
Design C	square

Table 1: Three design scenarios for the architectural shell roof. The labels refer to the vertices in Figure 9 whose coordinates are fixed during optimisation.

vertices is depicted in Figure 9. On the control mesh some of the vertices are tagged as *corner vertices* (empty squares) and some of the edges as *crease edges* (thick lines). At tagged vertices and edges locally modified stencils are applied during subdivision refinement, see [4, 27] for details. These stencils ensure that sharp corners and G^0 -continuous feature lines are preserved. The visual effect of the tagging on the limit surface in Figure 8 is evident. Moreover, the tags have an influence on the entries in the subdivision matrix \mathbf{S} , the coarsening matrix \mathbf{R} and the basis functions $N_i(\theta^1, \theta^2)$.

For shape optimisation three different design scenarios, referred to as Design A, Design B and Design C, are considered, see Table 1. Depending on the design scenario the positions of some of the highlighted vertices in Figure 9 are fixed during the optimisation iterations. The coarsest control mesh shown in Figure 9 for optimisation contains 26 vertices and the twice subdivided finite element mesh with $\ell_c = 2$ contains 272 vertices. The design variables in optimisation are the out-of-plane positions of the vertices. This choice ensures that the planform of the shell roof is preserved. Only the positions of vertices in levels $\ell_o = 0$ and $\ell_o = 1$ are optimised, in turn. The optimisation of the vertex positions in the second level results in surfaces with fine-scale oscillations and has been omitted. It is also necessary to restrict the surface area of the shell to $A \leq 1.2A_0$, where A_0 is the area of the original surface. The initial value of the compliance cost function is 31.36. Design C results in the most efficient optimised shape with a 79.13% reduction in cost, followed by Design B with a reduction of 38.88%. The total reduction in the most constrained Design A is only 23.97%. The corresponding optimised shapes for each design scenario are shown in Figures 10, 11 and 12. As can be seen in these figures the optimised Design C has more variation in the surface curvature, which usually leads to stiffer and less compliant structures. This variation of the curvature is especially pronounced in the large overhanging front part of the shell structure. Note also that on all surfaces the characteristic ridge feature and the sharp corners at both ends of the shell are preserved due to the use of extended subdivision schemes.

5.4. Conclusions

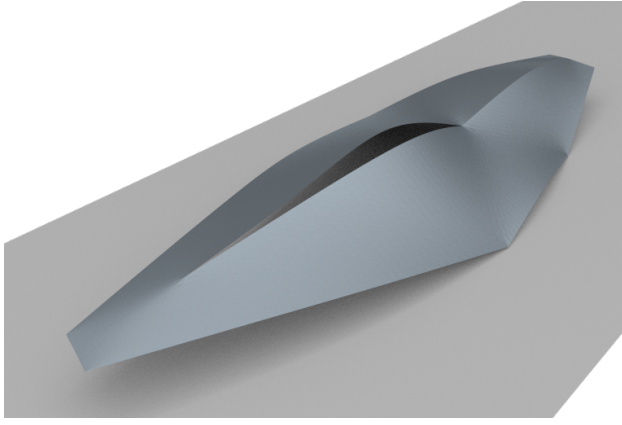
We introduced the isogeometric shape optimisation of shell structures using triangular Loop and quadrilateral Catmull-Clark subdivision surfaces as a common representation for geometric modelling and finite element analysis. The presented examples demonstrate that efficient and flexible representation of freeform shell geometries is essential for shape optimisation. In the implemented gradient-based shape optimisation approach more optimal geometries are obtained when, starting from the

coarsest control mesh, the vertices of increasingly finer control meshes are chosen as geometric design variables. Irrespective of the control mesh resolution for optimisation a sufficiently fine control mesh can always be used for finite element discretisation. In general the finite element control meshes have to be finer than the optimisation control meshes for accuracy reasons. The introduced approach effectively allows the designer to choose an optimal geometry with a visually pleasing and technically feasible smallest feature size. With the increasing availability of subdivision surfaces in CAD systems it is expected that it will become feasible to import the optimised geometries back into a CAD environment for continuing with the design process.

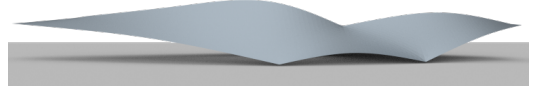
The presented isogeometric shape optimisation approach can be extended and improved in several ways. First, we considered only the structural compliance as a cost function and that for only one loading case. In practice, there are many more load cases and competing cost functions which have to be taken into account. For instance, the structural stability, i.e. buckling, of optimised thin shells is often critical and has to be taken into account [41]. Moreover, the geometric fidelity of the surfaces in the presented approach can be improved using more recent higher-degree subdivision surfaces, such as the NURBS-compatible subdivision surfaces [42], or adaptively refined subdivision surfaces [43, 44]. Finally, the multiresolution editing techniques from computer graphics based on wavelet-like decomposition of surfaces can be employed for interlacing geometry generation by the user with automated structural optimisation [30].

References

- [1] T. J. R. Hughes, J. A. Cottrell, Y. Bazilevs, Isogeometric analysis: CAD, finite elements, NURBS, exact geometry and mesh refinement, *Computer Methods in Applied Mechanics and Engineering* 194 (2005) 4135–4195.
- [2] J. A. Cottrell, T. J. R. Hughes, Y. Bazilevs, *Isogeometric Analysis: Toward Integration of CAD and FEA*, John Wiley & Sons Ltd., 2009.
- [3] F. Cirak, M. Ortiz, P. Schröder, Subdivision surfaces: A new paradigm for thin-shell finite-element analysis, *International Journal for Numerical Methods in Engineering* 47 (2000) 2039–2072.
- [4] F. Cirak, Q. Long, Subdivision shells with exact boundary control and non-manifold geometry, *International Journal for Numerical Methods in Engineering* 88 (2011) 897–923.
- [5] Q. Long, P. B. Bornemann, F. Cirak, Shear-flexible subdivision shells, *International Journal for Numerical Methods in Engineering* 90 (2012) 1549–1577.
- [6] J. Kiendl, K.-U. Bletzinger, J. Linhard, R. Wüchner, Isogeometric shell analysis with Kirchhoff-Love elements, *Computer Methods in Applied Mechanics and Engineering* 198 (2009) 3902–3914.
- [7] A. P. Nagy, M. M. Abdalla, Z. Gürdal, Isogeometric sizing and shape optimisation of beam structures, *Computer Methods in Applied Mechanics and Engineering* 199 (2010) 1216–1230.
- [8] E. J. Haug, K. K. Choi, V. Komkov, *Design Sensitivity Analysis of Structural Systems*, Academic Press, 1986.
- [9] P. Christensen, A. Klarbring, *An Introduction to Structural Optimization*, Springer, 2009.
- [10] R. T. Haftka, R. V. Grandhi, Structural shape optimization — a survey, *Computer Methods in Applied Mechanics and Engineering* 57 (1986) 91–106.
- [11] J. A. Samareh, Survey of shape parameterization techniques for high-fidelity multidisciplinary shape optimization, *AIAA journal* 39 (2001) 877–884.



(a) Perspective view.

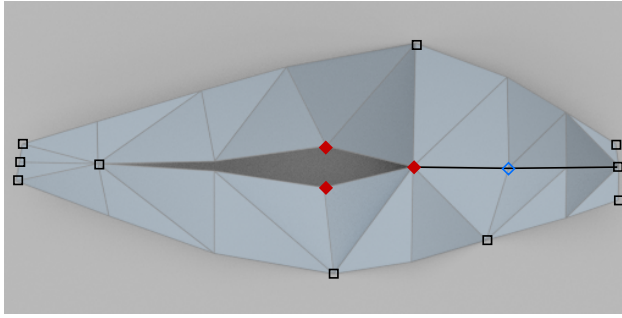


(b) Front view.

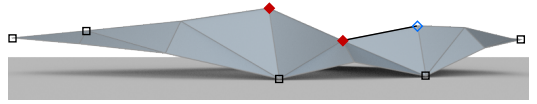


(c) Back view.

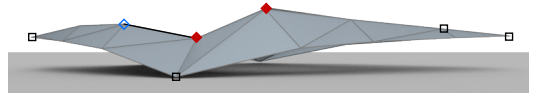
Figure 8: Freeform architectural roof supported at three points and containing a central opening and a creased ridge (with G^0 continuity). The corresponding coarse resolution control mesh is shown in Figure 9.



(a) Top view.

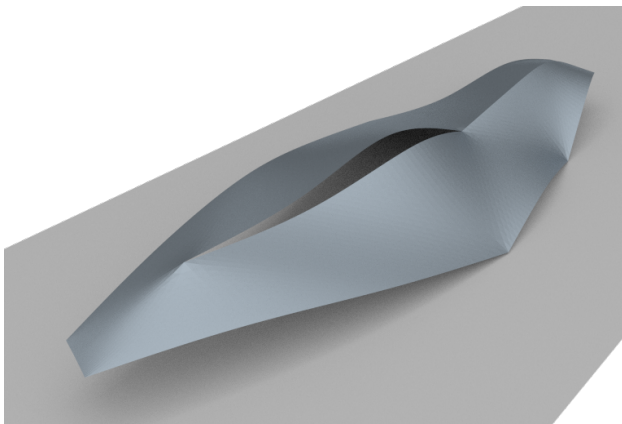


(b) Front view.

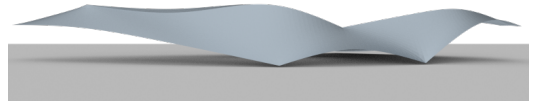


(c) Back view.

Figure 9: Triangular coarse control mesh with vertex and edge tags. The black square vertices indicate corner tags and the thick black edges indicate crease tags. The effect of the tagging on the limit surface can be observed in Figure 8. During the considered three optimisation design case studies (Design A, Design B and Design C) some of the vertex coordinates are fixed as specified in Table 1.



(a) Perspective view.

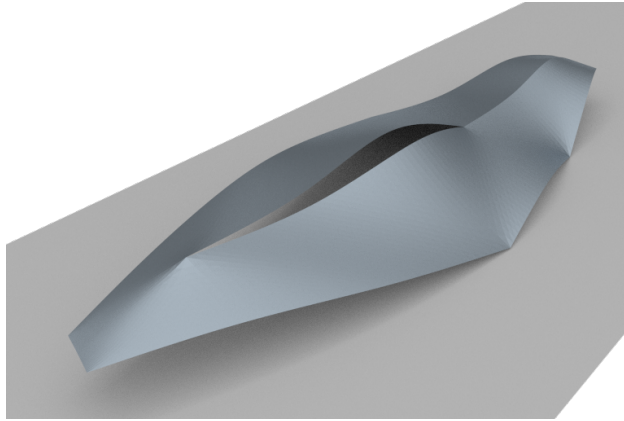


(b) Front view.

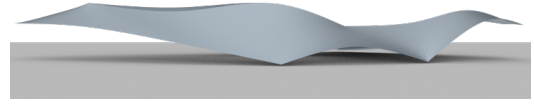


(c) Back view.

Figure 10: Limit surface of the optimised roof Design A. The final value of the compliance is 23.84 representing a 23.97% reduction.



(a) Perspective view.

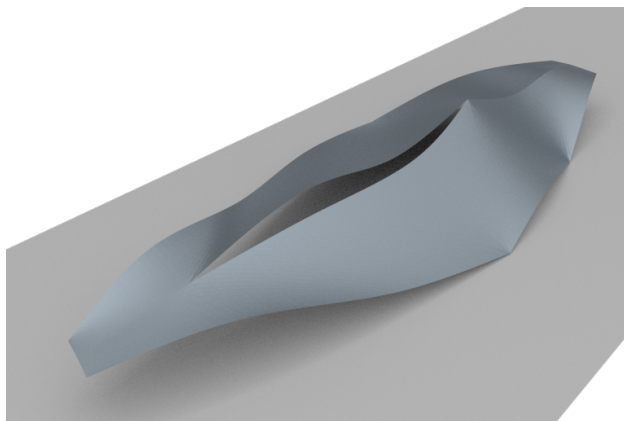


(b) Front view

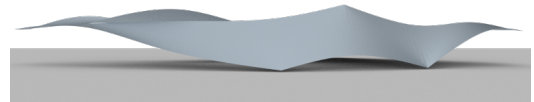


(c) Back view

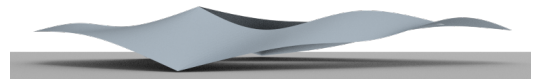
Figure 11: Limit surface of the optimised architectural roof Design B. The final value of the compliance is 19.17 representing a 38.88% reduction.



(a) Perspective view.



(b) Front view.



(c) Back view.

Figure 12: Limit surface of the optimised roof Design C. The final value of the objective function is 6.55 representing a 79.13% reduction.

- [12] V. Braibant, C. Fleury, Shape optimal design using b-splines, *Computer Methods in Applied Mechanics and Engineering* 44 (1984) 247–267.
- [13] K.-U. Bletzinger, E. Ramm, Form finding of shells by structural optimization, *Engineering with Computers* 9 (1993) 27–35.
- [14] E. Cervera, J. Trevelyan, Evolutionary structural optimisation based on boundary representation of NURBS. Part I: 2D algorithms, *Computers & Structures* 83 (2005) 1902–1916.
- [15] T. T. Robinson, C. G. Armstrong, H. S. Chua, C. Othmer, T. Grahs, Optimizing parameterized CAD geometries using sensitivities based on adjoint functions, *Computer-Aided Design and Applications* 9 (2012) 253–268.
- [16] X. Han, D. W. Zingg, An adaptive geometry parametrization for aerodynamic shape optimization, *Optimization and Engineering* 15 (2014) 69–91.
- [17] C. Le, T. Bruns, D. Tortorelli, A gradient-based, parameter-free approach to shape optimization, *Computer Methods in Applied Mechanics and Engineering* 200 (2011) 985–996.
- [18] M. Firl, R. Wüchner, K.-U. Bletzinger, Regularization of shape optimization problems using FE-based parametrization, *Structural and Multidisciplinary Optimization* 47 (2013) 507–521.
- [19] K.-U. Bletzinger, A consistent frame for sensitivity filtering and the vertex assigned morphing of optimal shape, *Structural and Multidisciplinary Optimization* 49 (2014) 873–895.
- [20] S. Jakobsson, O. Amignon, Mesh deformation using radial basis functions for gradient-based aerodynamic shape optimization, *Computers & Fluids* 36 (2007) 1119–1136.
- [21] M. H. Imam, Three-dimensional shape optimization, *International Journal for Numerical Methods in Engineering* 18 (1982) 661–673.
- [22] T. W. Sederberg, S. R. Parry, Free-form deformation of solid geometric models, *SIGGRAPH 1986 Conference Proceedings* 20 (1986) 151–160.
- [23] D. Zorin, P. Schröder, Subdivision for Modeling and Animation, *SIGGRAPH 2000 Course Notes*, 2000.
- [24] J. Peters, U. Reif, *Subdivision Surfaces*, Springer Series in Geometry and Computing, Springer, 2008.
- [25] C. T. Loop, *Smooth Subdivision Surfaces Based on Triangles*, Master’s thesis, Department of Mathematics, University of Utah, 1987.
- [26] E. Catmull, J. Clark, Recursively generated B-spline surfaces on arbitrary topological meshes, *Computer-Aided Design* 10 (1978) 350–355.
- [27] H. Biermann, A. Levin, D. Zorin, Piecewise Smooth Subdivision Surfaces with Normal Control, in: *SIGGRAPH 2000 Conference Proceedings*, New Orleans, LA, 113–120, 2000.
- [28] F. Cirak, M. J. Scott, E. K. Antonsson, M. Ortiz, P. Schröder, Integrated modeling, finite-element analysis, and engineering design for thin-shell structures using subdivision, *Computer-Aided Design* 34 (2002) 137–148.
- [29] K. Bandara, F. Cirak, G. Of, O. Steinbach, J. Zapletal, Boundary element based multiresolution shape optimisation in electrostatics, *Journal of Computational Physics* 297 (2015) 584–598.
- [30] K. Bandara, T. Rüberg, F. Cirak, Shape optimisation with multiresolution subdivision surfaces and immersed finite elements, *Computer Methods in Applied Mechanics and Engineering* 300 (2016) 510–539.
- [31] A. Wawrzinek, K. Polthier, Integration of generalized B-spline functions on Catmull–Clark surfaces at singularities, *Computer-Aided Design* 78 (2016) 60–70.
- [32] B. Jüttler, A. Mantzaflaris, R. Perl, M. Rumpf, On numerical integration in isogeometric subdivision methods for PDEs on surfaces, *Computer Methods in Applied Mechanics and Engineering* 302 (2016) 131–146.
- [33] M. Majeed, F. Cirak, Isogeometric analysis using manifold-based smooth basis functions, *Computer Methods in Applied Mechanics and Engineering* 316 (2017) 547–567.
- [34] J. Stam, Exact evaluation of Catmull–Clark subdivision surfaces at arbitrary parameter values, in: *SIGGRAPH 1998 Conference Proceedings*, Orlando, FL, 395–404, 1998.
- [35] J. Stam, Evaluation of Loop subdivision surfaces, in: *SIGGRAPH 1999 Course Notes*, Los Angeles, CA, 1999.
- [36] I. Boier-Martin, D. Zorin, Differentiable parameterization of Catmull–Clark subdivision surfaces, in: *Eurographics 2004 Conference Proceedings*, ACM, 155–164, 2004.
- [37] M. Antonelli, C. V. Beccari, G. Casciola, R. Ciarloni, S. Morigi, Subdivision surfaces integrated in a CAD system, *Computer-Aided Design* 45 (2013) 1294–1305.
- [38] S. G. Johnson, The NLOpt nonlinear-optimization package, <http://ab-initio.mit.edu/nlopt>.
- [39] E. H. Lockwood, *A book of curves*, Cambridge University Press, 1961.
- [40] E. Bradner, F. Iorio, M. Davis, Parameters tell the design story: ideation and abstraction in design optimization, in: *Proceedings of the Symposium on Simulation for Architecture & Urban Design*, 26, Society for Computer Simulation International, 2014.
- [41] R. Reitinger, E. Ramm, Buckling and imperfection sensitivity in the optimization of shell structures, *Thin-walled structures* 23 (1995) 159–177.
- [42] T. J. Cashman, U. H. Augsdörfer, N. A. Dodgson, M. A. Sabin, NURBS with extraordinary points: high-degree, non-uniform, rational subdivision schemes, in: *SIGGRAPH 2009 Conference Proceedings*, New Orleans, LA, 46:1–46:9, 2009.
- [43] X. Wei, Y. Zhang, T. J. R. Hughes, M. A. Scott, Truncated hierarchical Catmull–Clark subdivision with local refinement, *Computer Methods in Applied Mechanics and Engineering* 291 (2015) 1–20.
- [44] P. B. Bornemann, F. Cirak, A subdivision-based implementation of the hierarchical b-spline finite element method, *Computer Methods in Applied Mechanics and Engineering* 253 (2013) 584–598.